A topological approach for quantitative comparisons of ocean model fields to satellite ocean color data

Hannah R. Hiester[a,*], Steven L. Morey[a], Dmitry S. Dukhovskoy[a], Eric P. Chassignet[a], Vassiliki H. Kourafalou[b], Chuanmin Hu[c]

[a]Center for Ocean-Atmospheric Prediction Studies, Florida State University, 2000 Levy Avenue, Building A, Suite 292, Tallahassee, FL 32306-2741, USA.

[b]Rosenstiel School of Marine and Atmospheric Sciences, University of Miami 4600 Rickenbacker Causeway, Miami, FL 33149-1098, USA.

[c]Optical Oceanography Laboratory, College of Marine Science, University of South Florida, 140 7th Avenue S, MSL119, St. Petersburg, FL 33701, USA.

[*]Corresponding Author: hhiester@fsu.edu

Highlights

- A topological metric is introduced for comparing differing but related geophysical fields
- The metric is demonstrated by comparing satellite ocean color data to model salinity

- The metric allows quantitative comparison of spatial characteristics of observed and modeled fields

Key words: satellite data; ocean model; ocean color; sea surface salinity; shape comparison; hausdorff distance

Abstract

The aim of this work is to demonstrate a method for quantifying the agreement between time-evolving spatial features evident in fields of differing, but functionally related, variables that are more commonly compared qualitatively via visual inspection. This is achieved through application of the Modified Hausdorff Distance metric to the evaluation of ocean model simulations of surface salinity near a river plume using satellite ocean color data. The Modified Hausdorff Distance is a metric from the field of topology designed to compare shapes and the methodology provides quantitative assessment of similarity of spatial fields. The Modified Hausdorff Distance can be applied for comparison of many geophysical and ecological fields that vary spatially and temporally. Here, the utility of the metric is demonstrated by applying it to evaluate numerical simulations of the time-evolving spatial structure of the surface salinity fields from three ocean models in the vicinity of large riverine sources in the northeast Gulf of Mexico. Using the Modified Hausdorff Distance, quantitative comparison of modeled sea surface salinity contours to contours of a gridded satellite-derived ocean color product is made under the assumption that the modeled fields are related to optically significant quantities that indicate the spatial extent of riverine influenced water. Three different ocean models are evaluated and are compared individually to the satellite data. The sea surface salinity

values and ocean color index values that most closely match (lowest Modified Hausdorff Distance score) are identified for each model. The Modified Hausdorff Distance scores for these best pairings are used to both determine which model simulates surface salinity fields that most closely match the satellite observations and obtain an empirical relationship between the two variables for each model. Furthermore, the best pairings are compared between models allowing key differences in the simulated riverine water distributions to be distinguished. The Modified Hausdorff Distance proves a robust and useful diagnostic tool that has the potential to be utilized in many geophysical applications and facilitate the use of satellite ocean color data for quantitative evaluation of hydrodynamic ocean models.

1 Introduction

For decades satellite sensors have been used to detect the color of the ocean surface by measuring light reflectance in different spectral bands (McClain, 2009). These ocean color data products have been utilized to identify and analyze ocean features that affect pigment and particulate content of the water and hence the ocean color, including oil spills, algal blooms and river plumes (e.g. Hu et al., 2004; Androulidakis and Kourafalou, 2013; Liu et al. 2013; Hu et al., 2015a). They have also been integrated into observation and detection systems for harmful algal blooms and oil spills (e.g. Stumpf et al., 2003; Brekke & Solberg, 2005; Hu et al., 2015b). With both broad spatial and frequent temporal coverage, satellite ocean color observations also have the potential to be valuable resources for numerical ocean modeling, however the ocean circulation modeling community has not fully capitalized on the utility of this data.

Satellite ocean color data have been used for ocean model assessment qualitatively, as patterns evident in the ocean color are often similar to, and may generally be visually compared to, features in dynamical fields (e.g. Binding & Bowers, 2003; Gregg et al., 2003; Chassignet et al., 2006; Liu et al., 2011; Schiller et al., 2011). Quantitative comparisons generally rely on point-wise differences that demand the same field be used and/or an empirical relationship between different but related fields is determined (e.g. Binding & Bowers, 2003; Gregg et al., 2003; Gregg, 2008; Mariano et al., 2011; Chaichitehrani et al., 2014; Zhang et al. 2014). While the types of statistical measures derived from point-wise comparisons (e.g. biases or correlations) are useful, they do not necessarily provide comparison of spatial distributions and/or shape that are related to circulation patterns or dynamical processes, and neither are they expressly designed for such a purpose. The objective of this work is to apply and demonstrate the potential of a metric called the Modified Hausdorff Distance (MHD) to quantitatively compare spatial and temporal patterns derived from satellite ocean color observations to ocean circulation models in an effort to more fully utilize the vast amount of remotely sensed oceanographic data.

2 Background

The MHD originates from the field of topology and is designed specifically to compare shapes (Dubuisson & Jain, 1994). The MHD and Hausdorff distance, from which the former is derived, are frequently used in imaging software for object location and pattern recognition. (Huttenlocher et al., 1993; Huttenlocher & Rucklidge, 1993; Rucklidge, 1997; Daoudi et al., 1999; Zhang & Lu, 2004). There has been some application to analysis of geospatial data, an example being precipitation patterns where

88 the Hausdorff distance forms one component of a Forecast Quality Index (e.g. Venugopal
89 et al., 2005; Nan et al., 2010) and application of the MHD for skill assessment of sea ice
90 models based on analysis of spatial distribution of sea ice concentration (Dukhovskoy et
91 al., 2015). However, the metric has not been widely utilized in oceanographic
92 applications. The particular application considered here compares ocean model surface
93 salinity fields with satellite ocean color data near a large river source, the Mississippi
94 River. This presents the opportunity to utilize ocean color data from satellites for
95 quantitative model assessment and intermodel comparison in a region with high spatial
96 and temporal variability of the salinity field.

97 The Mississippi River enters the northeast Gulf of Mexico (NEGoM) through
98 several channels along the end of the Mississippi Delta. This study focuses on the area
99 east of the Mississippi Delta, where the shelf is nearly non-existent, and small mesoscale
100 deep ocean eddies dominate the circulation field over the nearby DeSoto Canyon. The
101 domain for the analysis presented here extends from approximately 50 km west of the
102 Mississippi Delta eastward to Apalachicola Bay in North Florida, and from 28°N
103 northward to the coast (Figure 1). The surface salinity in this region is influenced by
104 several rivers and is dominated by outflow from the Mississippi River (Figure 2). During
105 the fall and winter months, the Mississippi River plume tends to be trapped closely to the
106 coast westward of the study domain (Morey et al., 2003a; Morey et al., 2005). In the
107 spring and summer, reversal of the climatological wind allows the plume to spread
108 eastward over the DeSoto Canyon region (Morey et al., 2003b; Walker et al., 2005).
109 Interaction with circulation features such as the Loop Current and Loop Current Eddies
110 leads to a complex structure, with salinity contours forming intricate shapes with

(a)

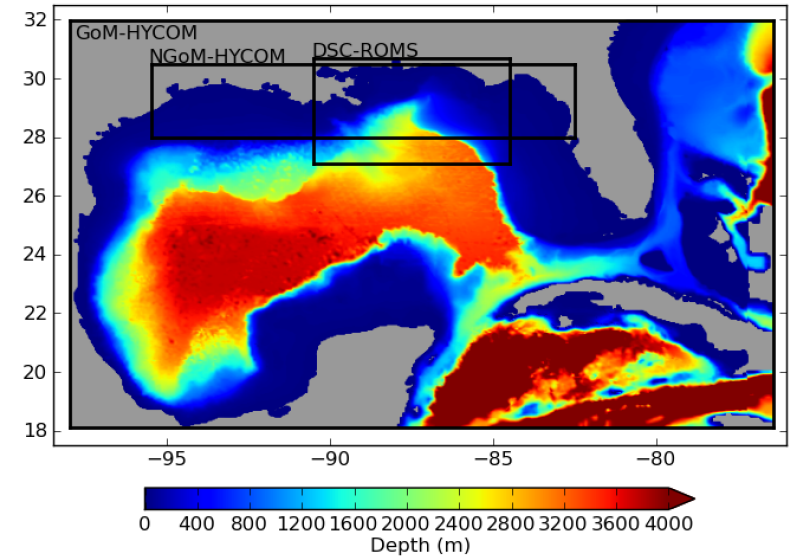

(b)

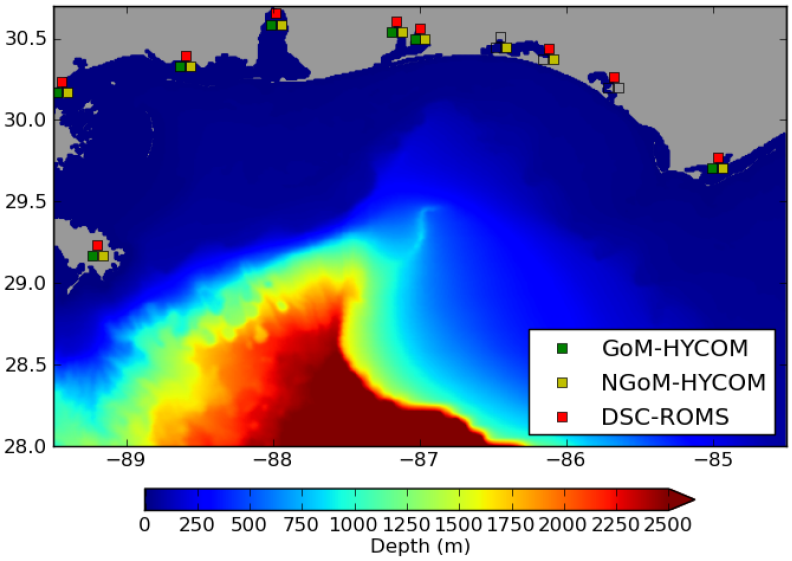

111

112 **Figure 1**: Bathymetry and model domains. (a) Full Gulf of Mexico. The bathymetry is shown
113 for GoM-HYCOM configuration. Boxes represent domains for the DSC-ROS and NGoM
114 HYCOM. (b) Subdomain common to all models used for analysis. The bathymetry is shown
115 for the DSC-ROMS configuration. The squares denote river sources that are simulated in
116 each model.

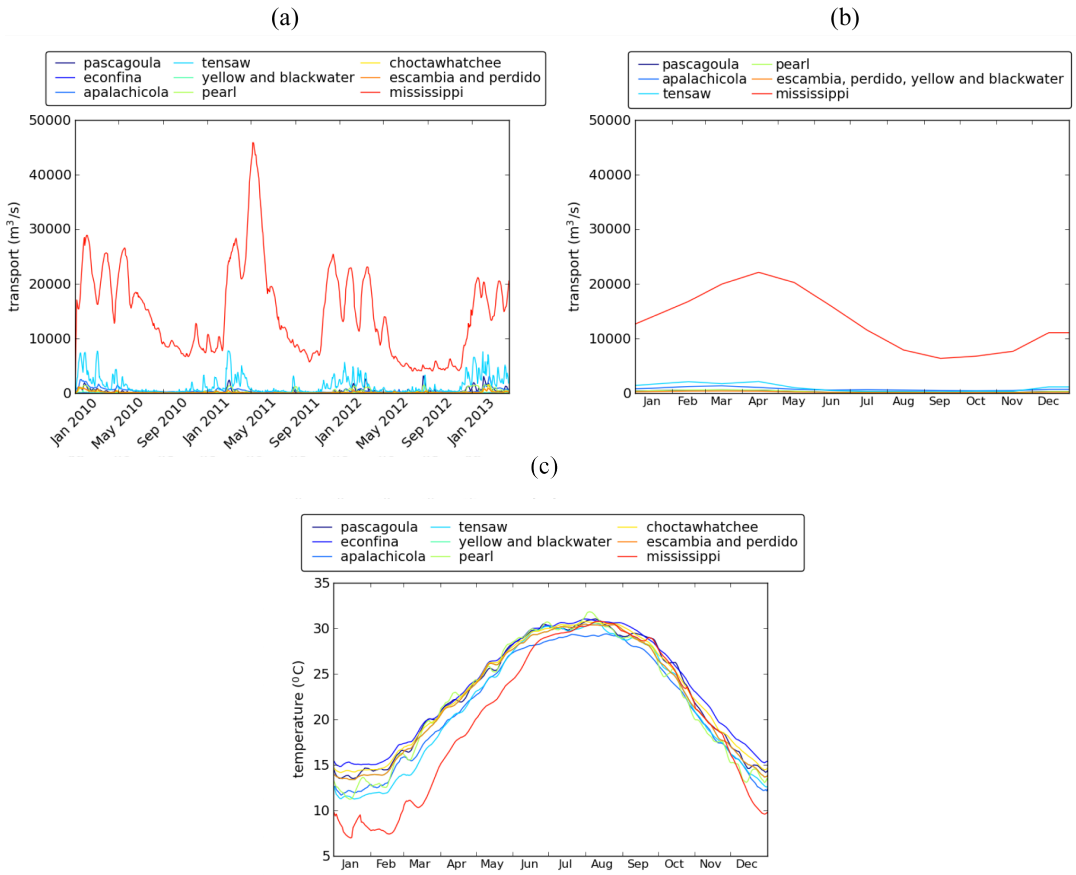

117

118 **Figure 2**: (a) Daily river discharge calculated from US Geological Survey data used for DSC-
119 ROMS transport. NGoM-HYCOM uses the same data source to calculate daily river transport
120 and has similar variation and magnitude. (b) Monthly climatology used for GoM-HYCOM
121 river transport. (c): Temperature climatology calculated from NOAA tides and currents data
122 used for DSC-ROMS. For river locations see Figure 1.

123 filaments extending across the domain (Figures 3 and 4, Walker et al., 1996; Morey et al.,
124 2003b; Schiller et al., 2011; Androulidakis & Kourafalou, 2013). The geometry of these
125 fields presents a challenging system for the MHD to assess, making the region and the
126 system analyzed an excellent scenario for demonstration and evaluation of the utility of
127 the metric.

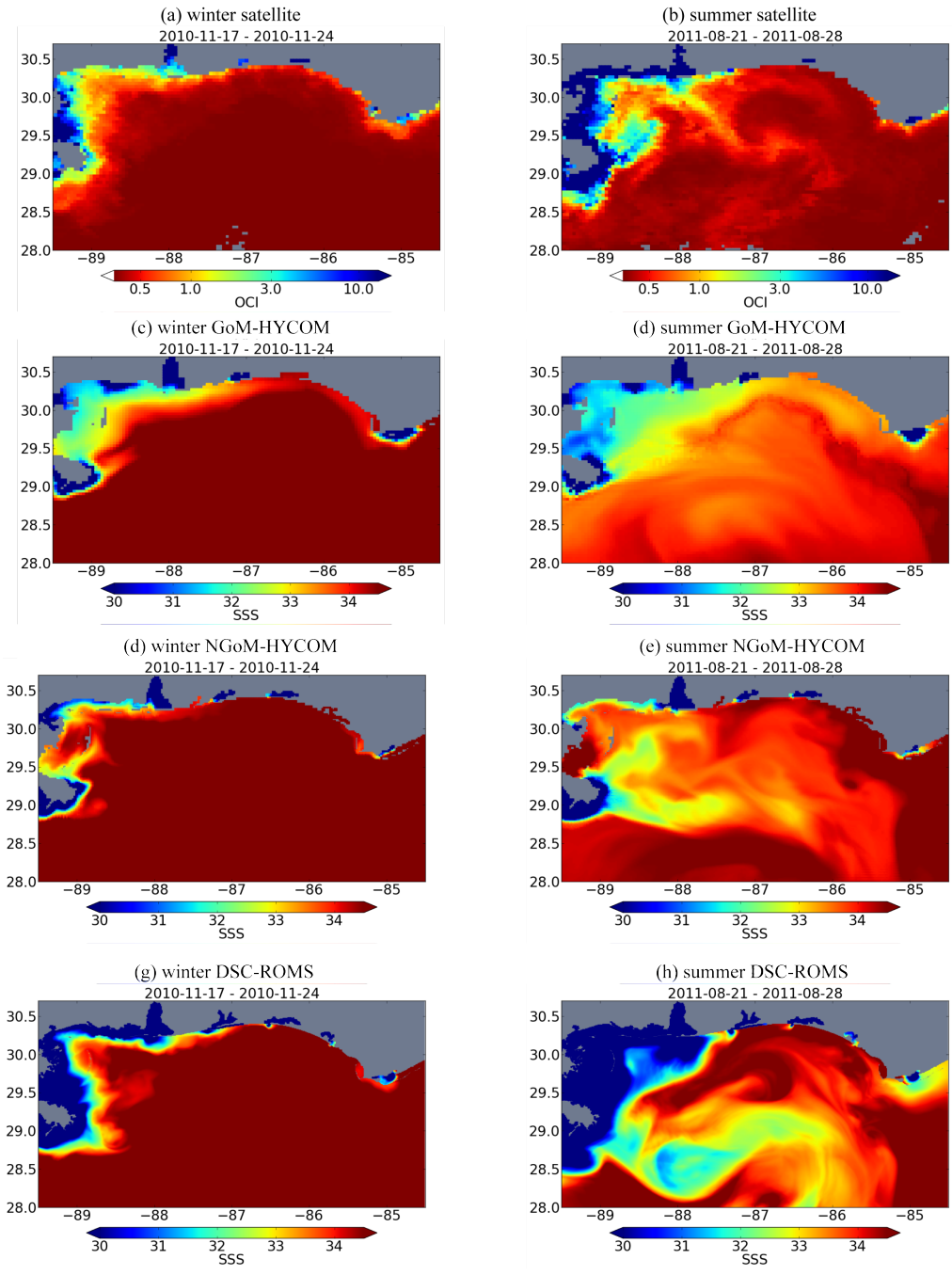

128

129 **Figure 3**: Example 8-day averaged fields of typical winter (left) and summer (right) OCI (a-
130 b) and SSS fields from GoM-HYCOM (c-d), NGoM-HYCOM (e-f) and DSC-ROMS (g-h).
131 In the winter, the riverine-influenced water is more coastally trapped. In the summer, the low
132 salinity/high OCI water spreads out over the region. Animations for the entire time periods
133 from each of the above can be found at:
134 http://coaps.fsu.edu/~hhiester/Satellite_colormap.mp4 (satellite),
135 http://coaps.fsu.edu/~hhiester/GoM-HYCOM_colormap.mp4 (GoM-HYCOM),
136 http://coaps.fsu.edu/~hhiester/NGoM-HYCOM_colormap.mp4 (NGoM-HYCOM) and
137 http://coaps.fsu.edu/~hhiester/DSC-ROMS_colormap.mp4 (DSC-ROMS).

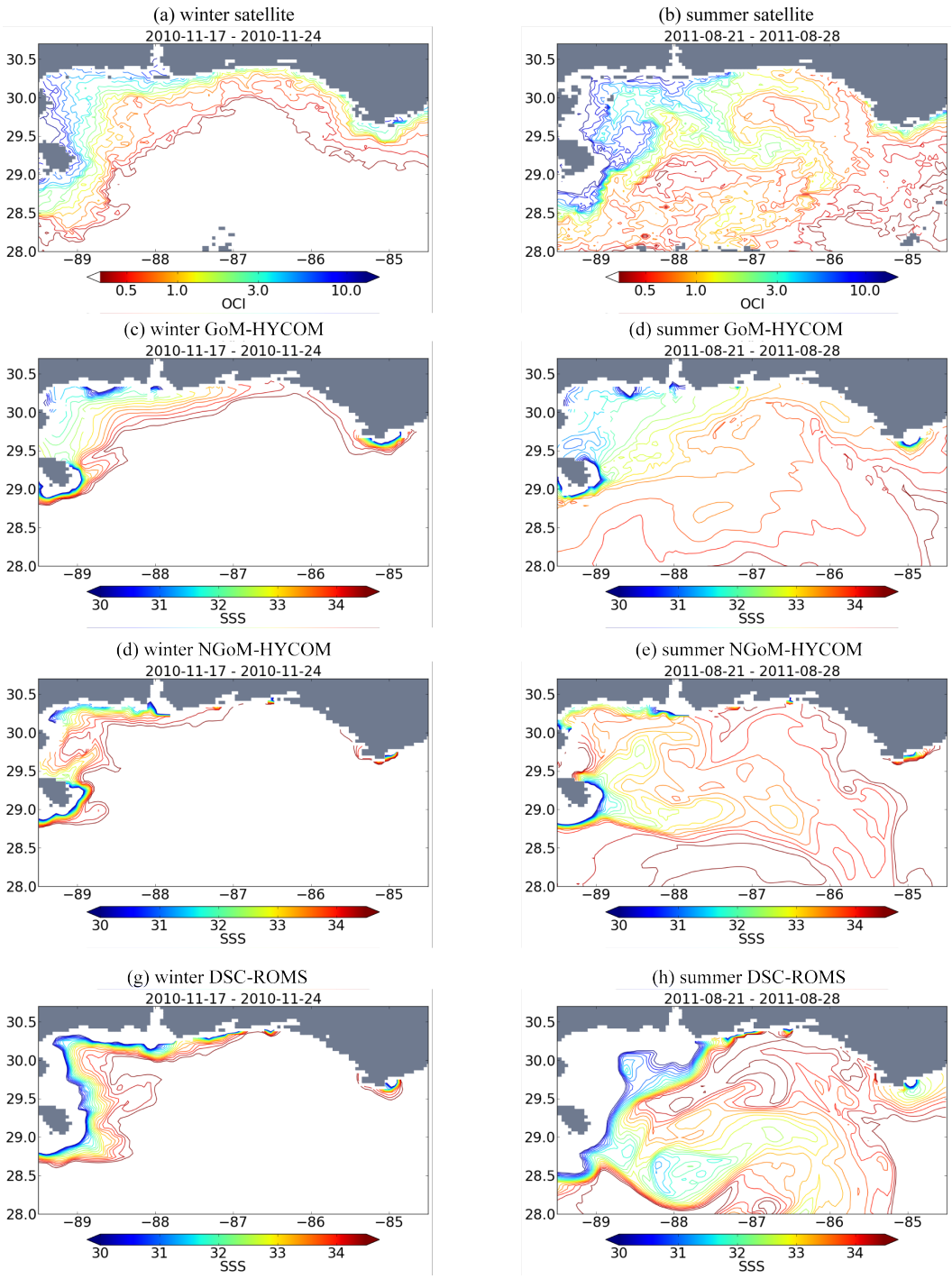

Figure 4: Examples of contours of the fields shown in Figure 3. The ocean model data have been regridded to the 4-km grid of the OCI product. Animations for each of the above can be found at:
http://coaps.fsu.edu/~hhiester/Satellite_contours.mp4 (satellite),
http://coaps.fsu.edu/~hhiester/GoM-HYCOM_contours.mp4 (GoM-HYCOM),
http://coaps.fsu.edu/~hhiester/NGoM-HYCOM_contours.mp4 (NGoM-HYCOM) and
http://coaps.fsu.edu/~hhiester/DSC-ROMS_contours.mp4 (DSC-ROMS).

3 Data and Methods

This study demonstrates application of the MHD for comparing satellite-derived and ocean model fields of different, but related quantities. In particular, an ocean color product derived from satellite optical data is compared to salinity fields from three different models to evaluate the models' representations of the distribution of riverine water. In this section, the MHD and Hausdorff distance (from which the MHD is derived) are introduced, the ocean color product and the model simulations are described, and the application of the MHD and diagnostic techniques are detailed.

3.1 The Hausdorff distance

The Hausdorff distance is a topological metric commonly used in the context of visual imaging for pattern recognition and shape matching, with utility for applications such as facial recognition (Huttenlocher & Rucklidge, 1993; Huttenlocher, et al., 1993; Rucklidge, 1997; Daoudi et al., 1999; Zhang & Lu, 2004). The Hausdorff distance is very sensitive to outliers within a data set and modified versions (the Modified Hausdorff Distance) of the metric that have a more robust response to both outliers and noise have been investigated (Dubuisson & Jain, 1994; Mattern et al., 2010). Here, following Dubuisson & Jain (1994) and Dukhovskoy et al. (2015), the version of the MHD used is given by

$$\mathrm{MHD} = max\{d(A,B), d(B,A)\}, \qquad (1)$$

where

$$d(A,B) = \frac{1}{|A|}\sum_{a\in A} d(a,B)\,;\; d(a,B) = inf_{b\in B} d(a,b), \qquad (2)$$

and

$$d(B,A) = \frac{1}{|B|}\sum_{b\in B} d(A,b)\,;\; d(A,b) = inf_{a\in A} d(a,b) \quad (3)$$

with *A* the set of points on one contour, *B* the set of points on a second contour and *d(a,b)* the distance between those points (here, great circle distance, km). In simple terms, it may be considered to be the largest of the average of the minimum distances between each point on contour A and contour B and the average of the minimum distances between each point on contour B and contour A. The MHD increases as the shapes become increasingly different and decreases as they become more similar. It is noted that the MHD is a topological distance and *d(a,b)* in equations 2 and 3 can be any appropriate distance depending on the application. However, in general, the value of the MHD should be viewed simply as a score with a lower value indicating a better match.

The version of the MHD above has been shown to outperform more traditional statistical approaches such as Root Mean Square Deviation and Mean Dispersion in sensitivity tests for rotation (within angles $<30^0$), translation, scaling and noise (Dukhovskoy et al., 2015). An appropriate response to these properties is an important component of application of the metric. Dukhovskoy et al. (2015) show an increase in MHD score as rotation and translation cause a greater difference in shape, which is desired for this application. For river plume comparison, orientation and location of certain features (e.g., filaments) in surface salinity contours are important characteristics and manifest as differences in rotation (orientation) and translation (location) of contours.

185 Dukhovskoy et al. (2015) also show that the MHD is robust to noise, with
186 contours being shown to be similar (small MHD score) if the amplitude of the noise is
187 small but also showing an increase in the MHD score (i.e. a difference in the contours) as
188 the amplitude of the noise grows larger. Robustness to noise is a very useful property for
189 comparing river plumes. If small-scale features (small-amplitude noise) are diffused and
190 therefore smoothed out of the contours of one model relative to the contours of another
191 slightly less diffuse model, then ideally a metric will still be able to determine whether
192 there is a general similarity in shape between the two sets of contours. At the same time,
193 if one model is notably more diffusive than another such that the plume shape and hence
194 contours are warped significantly in the diffuse case relative to the less diffusive case (i.e.
195 large-amplitude noise in the diffuse case), the metric should be able to determine that
196 there is a lack of similarity between the two and return a larger MHD score.

197 **3.2 Satellite Ocean Color Index**

198 An Ocean Color Index (OCI, Hu et al., 2012) derived from data from the Moderate
199 Resolution Imaging Spectroradiometer (MODIS) is used as a proxy identifying riverine
200 influenced water to evaluate the ocean model salinity fields in the vicinity of the
201 Mississippi River. The algorithm is based on a three-band subtraction for relatively clear
202 waters (chlorophyll a concentration < 0.25 mg m^{-3}), but switches to a blue/green band
203 ratio algorithm for more productive waters. These MODIS data were obtained from the
204 NASA Goddard Space Flight Center (GSFC, http://oceancolor.gsfc.nasa.gov) and
205 processed with the most current algorithms. This OCI product has 4km resolution and is
206 temporally averaged over eight days.

In addition to fresh water, rivers discharge suspended sediment, Colored Dissolved Organic Matter (CDOM), and nutrients that facilitate primary productivity (chlorophyll-rich phytoplankton growth). Relationships between CDOM and SSS have been previously shown using *in situ* data and used to harness satellite data to investigate oceanographic and esturaine waters (e.g. Hu et al., 2003; Green & Sosik, 2004; Chaichitehrani et al., 2014; Chonga et al., 2014). However, from the perspective of algorithms, it is difficult to derive an accurate CDOM product in riverine waters due to a number of reasons (e.g., uncertainties in atmospheric correction in the blue bands). As an alternative to a satellite CDOM product, the OCI is derived from an empirical algorithm that accounts for both phytoplankton and CDOM thus making it a good proxy for representation of the riverine water in the domain (Hu et al., 2004). As a river plume spreads and mixes with ambient seawater, concentrations of suspended sediment, CDOM and often phytoplankton decrease resulting in a decrease in OCI. Hence, a higher OCI tends to correspond to fresher water near the river mouth (i.e. a lower SSS value) and vice versa. Because OCI contains information about both CDOM and phytoplankton in offshore waters where suspended sediments are low, it is therefore reasonable to assume that there is a correspondence between OCI and SSS, particularly in the CDOM rich riverine waters.

3.3 Numerical Models

Three ocean model simulations are evaluated, two of which use the Hybrid Coordinate Ocean Model (HYCOM) and one of which uses the Regional Ocean Modeling System (ROMS). They differ in numerical methods and configuration. Of particular relevance are differences in data assimilation (assimilative or not), as this impacts representation

230 particularly of the mesoscale features in the domain that have been shown to impact
231 riverine water spreading in the NEGoM (e.g. Morey et al, 2003b; Schiller et al., 2011);
232 horizontal spatial resolution, which can impact both representation of fields and
233 horizontal mixing; surface forcing, particularly as the wind patterns have been shown to
234 impact riverine water distribution in the NEGoM (e.g. Morey et al., 2003a; 2003b); and
235 parameterization of river inflow. This information is summarized in Table 1. For further
236 information, the reader is directed to the cited references and references therein.

Table 1. Summary of the three model simulations.

Simulation	**GoM-HYCOM**	**NGoM-HYCOM**	**DSC-ROMS**
Data-assimilation	Data-assimilative	Free-running	Free-running
Horizontal resolution	1/25°	1/50°	1km
River parameterization	Surface freshwater flux with enhanced vertical diffusivity	Surface freshwater flux with enhanced vertical diffusivity and barotropic adjustment	Temperature, salinity and momentum point source (or series of point sources).
Surface forcing	NOGAPS	COAMPS	CFSR

237

238 **3.3.1 The Gulf of Mexico Hybrid Coordinate Ocean Model**

239 The Hybrid Coordinate Ocean Model (HYCOM) is a finite-difference primitive equation
240 hydrostatic ocean circulation model (Bleck, 2002; Chassignet et al., 2003; Chassignet, et
241 al., 2006). It incorporates a flexible vertical coordinate system allowing smooth transition

between isopycnal, terrain-following (sigma) and pressure coordinates to meet the demands of different ocean modeling challenges, for example complex bathymetry or changing stratification. HYCOM is used operationally by the US Navy and National Ocean Atmospheric and Administration (NOAA) in the global ocean forecasting systems (Chassignet et al., 2009; Metzger et al., 2014). In this paper, a data-assimilative HYCOM Gulf of Mexico hindcast product is evaluated and will be referred to as GoM-HYCOM. The archived data were obtained from the HYCOM server (HYCOM-31.0, http://hycom.org/data/goml0pt04/expt-31pt0). The domain encompasses the full Gulf of Mexico, [-98°W, -76.4°W] and [18.9°N, 31.96°N] in longitude and latitude respectively (Figure 1). The horizontal resolution is (1/25)° of longitude by (cos(latitude)/25)° in latitude resulting in grid spacing of approximately 3.8-4.2 km. 20 vertical layers are used transitioning in the open ocean from pressure levels in the mixed layer to isopycnals below and with sigma coordinates used in shallow water. The model is forced at the lateral open boundaries with climatology fields derived from a 1/12° HYCOM model simulation of the Atlantic Ocean (Kourafalou et al., 2009). The surface forcing is provided by the Navy Operational Global Atmospheric Prediction System (NOGAPS, Rosmond et al., 2002). Data-assimilation is incorporated using the Navy Coupled Ocean Data Assimilation (Cummings, 2005). River runoff is specified at 40 locations along the coast using a monthly climatology. The river input is implemented as a virtual salt flux at the surface (Huang, 1993; Schiller & Kourafalou, 2010). The virtual salt flux, S_f, is calculated from precipitation (P), evaporation (E) and river input (R), with $S_f=[-(P-E)-R]S/\alpha_0$ where S is the salinity in the top layer of the model and α_0 is a reference specific volume. S_f is then used to calculate the salinity increment in the top

layer of the model, $dS = S_f dt_{bclin}\, g/dp$ where dt_{bclin} is the baroclinic time step, g is gravity and dp is the layer thickness in pressure units. At each baroclinic time step, the salinity in the top layer of the model, S, is updated to account for changes due to freshening via the virtual salt flux as $S(t+dt_{bclin}) = S(t) + dS$ where t is time. For each river, the freshwater flux is distributed over several ocean grid points adjacent to the river source and an enhanced diffusivity is employed over a depth of 6m to mix the source water through the water column. The surface salinity is relaxed to climatology.

3.3.2 The Northern Gulf of Mexico Hybrid Coordinate Ocean Model

A northern Gulf of Mexico free-running (non-assimilative) configuration of HYCOM (NGoM-HYCOM) has been developed (Schiller et al., 2011; Androulidakis & Kourafalou, 2013; Kourafalou and Androulidakis, 2013) with an advanced river input representation that extends the standard HYCOM code (section 3.3.1) to include momentum fluxes (in addition to salt fluxes) at the river mouth and the ability to distribute the river input both vertically at the river mouth and across estuarine cells (Schiller & Kourafalou, 2010). The domain extends across the Louisiana-Texas shelf and the Mississippi-Alabama-Florida shelf [-95.52 °W, -82.52°W] and [27.98°N, 30.70°N] in longitude and latitude respectively (Figure 1) and has 1/50° horizontal resolution. 30 vertical layers are used, 15 of which are fixed in the upper 40m of the water column. The model is nested in the 1/25° data-assimilative Gulf of Mexico HYCOM model (section 3.3.1) and atmospheric forcing is derived from the Coupled Ocean/Atmospheric Mesoscale Prediction System (COAMPS, Hodur et al. 2002). Daily average freshwater discharges derived from United Stated Geological Survey data are prescribed for 16 rivers, with monthly climatologies imposed for the Pearl River and Mobile Bay. These

289 rivers are specified as point sources (or multiple point sources for the Mississippi River)
290 and there is no relaxation to climatology. In addition, the barotropic pressure change of
291 the water column is adjusted to take into consideration the additional pressure exerted by
292 the additional mass, and hence volume, of the river inflow.

293 ### 3.3.2 The Regional Ocean Modeling System northeast Gulf of Mexico
294 configuration

295 The Regional Ocean Modeling System (ROMS) is a finite-difference primitive equation
296 ocean circulation model that employs the hydrostatic and Boussinesq approximations
297 (Shchepetkin & McWilliams, 2003; Shchepetkin & McWilliams, 2005). ROMS uses
298 sigma coordinates in the vertical that can be stretched to allow increased resolution in
299 areas of interest (Song & Haidvogel, 1994).

300 The ROMS configuration's domain encompasses the De Soto Canyon region in the
301 northeast Gulf of Mexico (Figure 1) and will be referred to as DSC-ROMS
302 (https://data.gulfresearchinitiative.org/data/R1.x138.080:0022/). The domain extends
303 from the Mississippi Delta to Apalachicola Bay [-90.5°W to -84.5°W] and [27.1°N to
304 30.7°N] in longitude and latitude respectively. 1 km resolution is used in the horizontal
305 and 40 layers are used in the vertical with stretching designed to increase resolution near
306 the surface and the upper part of the water column. The model is nested in the 1/12°
307 data-assimilative global HYCOM model and atmospheric forcing is derived from the
308 Climate Forecast Reanalysis System (CFSR, Saha et al. 2010). The river input is treated
309 as source terms for temperature, salinity, and momentum distributed vertically. Daily
310 average discharges are calculated from US Geological Survey data while temperature
311 climatology is calculated from NOAA tides and currents buoy data (Figure 2).

3.4 Diagnostics

3.4.1 Procedure overview

Two-dimensional contours (isolines) of select values are computed from the satellite OCI fields and SSS for each of the ocean models. The OCI generally decreases from the river sources as the riverine waters spread and mix with seawater. Conversely, the SSS values generally increase with distance from the river sources as the fresh river water mixes with the saline ambient water. These fields are thus indicators of the region influenced by riverine water, and the similarity of their spatial patterns is quantified using the MHD metric. Conducting this analysis on multiple pairings of values of SSS and OCI contours identifies the SSS-OCI relationships for each model and the differences in these pairings are utilized to compare the river plume representations between models.

3.4.2 Preprocessing

The satellite product and model data have differing time resolution, spatial resolution, and spatial domain bounds. To compare these data sets, the coarsest common temporal and spatial resolutions are adopted and the smallest common spatial domain is used (Figure 1). (When determining common spatial domains, regions of the nested NGoM-HYCOM and DSC-ROMS in which relaxation to the parent model fields takes place are not considered as part of the model domains for analysis purposes.) The satellite OCI dataset used in this study has the coarsest temporal resolution of the datasets with an eight-day average, as well as the coarsest spatial resolution with 4 km grid spacing. Therefore, the model data are temporally averaged over eight days and regridded to the satellite product's 4km grid using a nearest neighbor average. The land and cloud masks from the satellite data are then applied such that only areas with data present in all

products are compared at each time. The smallest common spatial domain is determined by the DSC-ROMS model for the eastern and western boundaries and the NGoM-HYCOM for the southern boundary. The northern boundary is bounded by the Mississippi-Alabama-Florida coastline. The resultant domain bounds used are therefore [-89.5°W,-84.5°W] and [28°N, 30.7°N] in longitude and latitude respectively, and only contours within this region are compared.

3.4.3 Application of the Modified Hausdorff Distance

To compare the models with the satellite data, the similarity between contours of OCI from the satellite data and contours of SSS from each of the models is quantified by calculating the MHD. An example of a satellite OCI field and a model SSS field and corresponding MHD values for pairs of SSS-OCI contours at a particular time are shown in Figure 5. As the SSS increases, the value of the OCI with the smallest MHD increases reflecting the inverse relationship between SSS and OCI (Figure 5c). In this example, fresher (higher OCI) contours are found closer to the coastline where they are similar in shape leading to smaller MHD values. Further from the shore, the higher salinity (lower OCI) contours have more complex shapes that are less similar and the MHD values for OCI-SSS pairings that most closely match reflect this lack of similarity by increasing correspondingly.

While both are good indicators of riverine-influenced water, the functional relationship between SSS and OCI values is not known. To determine this relationship empirically for each models' SSS field, the MHD is calculated for all pairs of OCI-SSS contour values, as shown by the example in Figure 5. The MHD values are then averaged

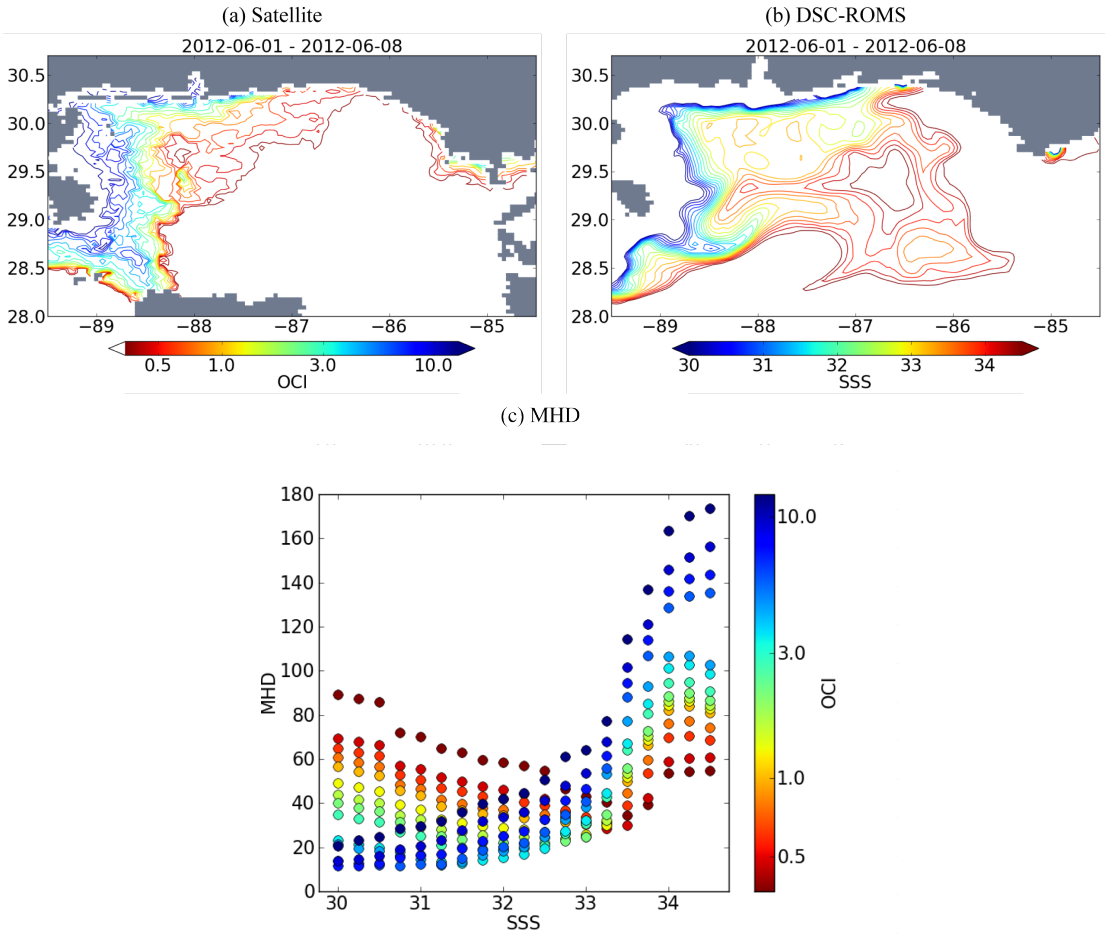

Figure 5. Contours of satellite OCI (a) and SSS from the DSC-ROMS (b) for a particular 8-day average (1-8 June 2012). (c) The corresponding MHD values for each SSS-OCI pair, with SSS on the horizontal axis and OCI value indicated by marker color. A smaller MHD indicates a better correspondence between the SSS and OCI contours. There is a decrease in OCI values associated with lowest MHD for each SSS value with increasing salinity, suggestive of an OCI-SSS functional relationship. Smaller values of MHD scores for the best pairings are found for lower SSS and higher OCI values, as these values are indicative of waters closer to the shore and river source where there is less spatial variation in the contours. Higher SSS and lower OCI values are generally found further from the coast where the contours are less similar in shape and location as demonstrated by higher MHD scores.

368 over time for each OCI-SSS pairing. The best pairings (lowest MHD) over all times are
369 then identified and a polynomial is fit to these data. This yields an empirical functional
370 relationship between SSS and OCI for each model. Inspection of the MHD for these
371 optimum OCI-SSS pairings also provides information about the model agreement with
372 the satellite data.

373 **3.4.4 Areal Coverage**

374 To compare with the MHD analysis, the sizes of the areas enclosed by various
375 surface salinity contours around the river source are calculated. Inspection of synoptic
376 fields of the SSS in the region suggests that the area contained within select contours of
377 SSS may be a good indication of the area influenced by the riverine waters at a given
378 time (Figure 4). Dukhovskoy et al. (2015) show that this metric performs poorly when
379 trying to rank models by shape because very different shapes may have the same area.
380 While it may not be suitable for distinguishing shape, the area metric can still be applied
381 to ascertain differences among model simulations of fresh riverine water near the surface.
382 For each model the area of water in the domain with SSS less than 30.0 and 34.5 (the
383 lowest and highest SSS values considered in the MHD analysis) are calculated. These
384 areas are then compared, both between models and to the analysis of the best OCI-SSS
385 pairings as determined by the MHD analysis.

386 **4 Results**

387 **4.1 Qualitative representation of the plume**

388 The seasonality of surface salinity in the region, characterized by summer
389 spreading and winter retraction (Walker et al., 1996; Morey et al., 2003a; Androulidakis

390 & Kourafalou, 2013) is evident in the satellite OCI and model SSS contours (Figures 3
391 and 4). During the fall and winter OCI and SSS contours are often compacted near the
392 coast as northwestward prevailing winds drive a coastally trapped current. During the
393 spring and summer, generally northward winds allow spreading to the east consistent
394 with Ekman drift, where mesoscale circulation features over this deeper region can
395 transport the low salinity water further south (Morey et al., 2003b). Features such as
396 filaments and smaller scale structures and undulations in the contours can be seen in the
397 model SSS and OCI contours at the 4 km resolution, although model fields have
398 increased complexity at their higher native resolutions.

399 In general, the near shore riverine waters correspond to values of OCI of 5 and
400 above. Further from the Mississippi Delta (the far field), values of OCI less than 0.35
401 approach the values of the ambient Gulf of Mexico waters making the full extent of the
402 river plume difficult to distinguish. The optical properties of the offshore waters of the
403 Gulf of Mexico have a distinct seasonal cycle largely due to changes in the mixed layer
404 (e.g. Muller-Karger, et al., 2015). OCI values between 0.37 and 12.19 are taken to be
405 representative of riverine water in the region and 15 values in this range, selected
406 incrementally on a logarithmic scale, are compared to model SSS contours.

407 Contours of SSS values from 30-34.5 with increments of 0.25 are computed from
408 the re-gridded model data. This range spans waters from the edges of the near field plume
409 to the outer far field where riverine waters have largely mixed with the open ocean waters
410 and approach the ambient salinity of the offshore Gulf of Mexico. The structure of the
411 plume varies between the models (Figures 3 and 4): GoM-HYCOM, the coarsest native
412 resolution model with climatological river forcing, generally has a broad spread of

smoother contours, with little clustering and few small scale variations. NGoM-HYCOM and DSC-ROMS, with increased native resolution and high frequency river forcing, show some additional detail in the contours and smaller scale features such as filaments. DSC-ROMS tends to have more of the lower salinity riverine water pushed further offshore compared to the GoM-HYCOM and NGoM-HYCOM in which the lower salinity riverine water does not generally extend as far offshore.

4.2 Comparison of MHD scores between models

The MHD scores for all OCI-SSS contour pairings are calculated for each model and each eight-day segment for the time period February 2010-February 2013, the longest time common to all data sets. For each of the 285 OCI-SSS pairings per model, the MHD scores are averaged over time resulting in one MHD score per pair per model (Figure 6 a-c). For a given SSS, the OCI value that yields the minimum MHD score (i.e. best match) can be identified (and vice versa). This provides a set of best pairings that can be compared between models. It should be noted that there is not an exact one-to-one correspondence between the pairings based on minimum MHD distances computed for each SSS contour and for each OCI contour. This is due to the spacing between values of the SSS and OCI contours chosen for this analysis. For example, in one region, several SSS contours may cluster in between more widely spaced OCI contours. The OCI contours will only be closest in shape to one SSS contour but two SSS contours may have the same OCI contour that is closest in shape. As the resolution of the SSS and OCI space increases, this discrepancy in the correspondence will likely decrease. However, using a substantially finer resolution of the SSS and OCI values will increase the computational

435 cost of the analysis given the already large number of combinations tested for each of the
436 three models over the three year period.

437 For the best pairings, the minimum MHD scores range from 20-40 km (Figure 6d)
438 with smaller values for the GoM-HYCOM and NGoM-HYCOM than DSC-ROMS by
439 approximately 5-15 km. This indicates a better correspondence of GoM-HYCOM and
440 NGoM-HYCOM simulated SSS spatial patterns with the satellite OCI data across a broad
441 range of OCI values. The exception is for very low salinity and high OCI values, where
442 DSC-ROMS has lower MHD scores.

443 The OCI-SSS value pairs that give the best MHD scores are not the same for each
444 model. Variations among the best OCI- SSS pairings can be used to analyze the
445 differences between riverine water distributions and salinity biases between models.

446 **4.3 SSS and OCI relationships**

447 The optimal pairings, identified by the minimum MHD scores, are compared
448 between models (Figure 6). For a specified SSS value, a lower OCI value for the model
449 in the best pairings indicates that the SSS contours are generally further offshore when
450 compared to the other models and vice versa. Alternatively, for a specified OCI value, a
451 lower SSS value in the best pair for a model indicates that model has a low SSS bias
452 relative to the other models.

453

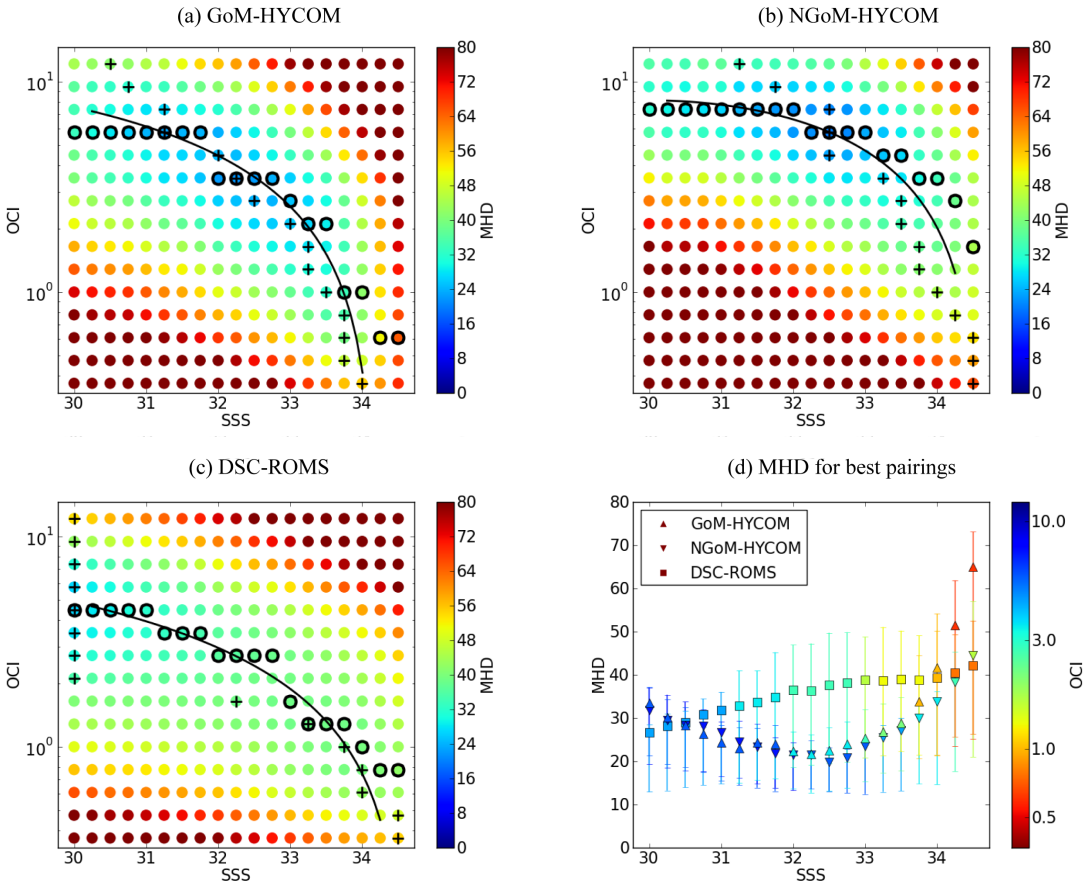

454

455 Figure 6: (a)-(c): Time averaged MHD values (indicated by the color of each dot) for each
456 SSS-OCI pairing for each model. Black circles represent the OCI value at which the MHD is
457 minimum for a given SSS and the black crosses represent the SSS value at which the MHD is
458 minimum for a given OCI. These symbols, therefore, represent the best pairings, as
459 determined by the MHD, and can be interpreted for each model as OCI as a function of SSS
460 (black circles), or SSS as a function of OCI (black crosses). The back lines show the
461 monotonic quadratic fit (Appendix A) to the best pairings for each model (excluding values at
462 the limits of the ranges of OCI and SSS contours tested). (d): The MHD for each SSS and
463 corresponding best match OCI value. These MHD values are generally smaller for GoM-
464 HYCOM and NGoM-HYCOM than DSC-ROMS indicating a better correspondence with the
465 OCI data, except for very low salinities where the DSC-ROMS SSS contours more closely
466 match the OCI data.

DSC-ROMS has a lower OCI for a given SSS (and lower SSS for a given OCI) when compared to GoM-HYCOM and NGoM-HYCOM. Therefore, DSC-ROMS tends to simulate fresher water further offshore and tends toward a low SSS bias in this region compared to the other models. At the other end of the spectrum, analysis of the NGoM-HYCOM yields the highest OCI for a given SSS, and higher SSS for a given OCI. Therefore, the model tends to have a high SSS bias relative to the other models over this region of freshwater influence. Thus, overall, from DSC-ROMS to GoM-HYCOM to NGoM-HYCOM the salinity bias moves from fresher to more saline.

All model river representations show a transition from high to low SSS as OCI increases. Considering SSS as a function of OCI defined by the best pairings (Figure 6), the SSS values change very abruptly over OCI values from 1 to 2 for DSC-ROMS indicating a more rapid variation in SSS, or a more compact salinity front, compared to the other two models. Furthermore, the transition from low to high salinity water begins at a lower OCI (further from the river source) for DSC-ROMS than for GoM-HYCOM and NGoM-HYCOM. GoM-HYCOM displays a broader transition over a wider range of OCI values than NGoM-HYCOM indicating less defined fronts. This is expected given the lower resolution of GoM-HYCOM, its specification of river input from climatology as opposed to daily measured discharge rates and parameterization of rivers using surface salinity relaxation.

Empirical functions describing the relationship between SSS to OCI were derived from the best pairings for each model (Appendix A). For each model, a quadratic function is fit to all of the best pairings including both those derived from the OCI that yields the minimum MHD for a given SSS and those derived from the SSS that yields the

minimum MHD for a given OCI (more detail may be found in Appendix A). The functions generally indicate a faster rate of change of OCI with SSS at higher SSS values for NGoM-HYCOM and GoM-HYCOM than for the DSC-ROMS simulation (Figure 6). This may be an indication of generally enhanced lateral mixing in the HYCOM simulations compared to the ROMS simulation.

A picture of the differences in the plumes can be built from the MHD analysis, with DSC-ROMS simulating a large area of low salinity water with a sharp transition to high salinity water and GoM-HYCOM displaying a broader transition from low to high salinity water. NGoM-HYCOM tends towards lower SSS values than GoM-HYCOM, and the riverine water does not spread as far across the domain in NGoM-HYCOM compared to GoM-HYCOM. These characteristics are further corroborated by analysis of the areal extent of low salinity waters that follows.

4.4 Areal extent of low salinity water

Visual inspection of model SSS contours (Figure 4) suggests that there are systematic differences between models in the area of very low salinity water (SSS<30) and overall amount of riverine-influenced water (SSS<34.5). This is confirmed quantitatively in the analysis of the SSS-OCI pairings (Figure 6) discussed in Section 4.3. To further characterize this aspect of the model salinity fields, the area of the ocean model surface with salinities less than prescribed thresholds are computed for each 8-day time-averaged field (Figure 7). DSC-ROMS has the largest area of very low salinity water (SSS<30.0) at all times. This is consistent with the greater spreading of the riverine water offshore diagnosed from the SSS-OCI pairing analysis. The total area of riverine-influenced water (as defined by SSS<34.5) is greatest for GoM-HYCOM, followed by

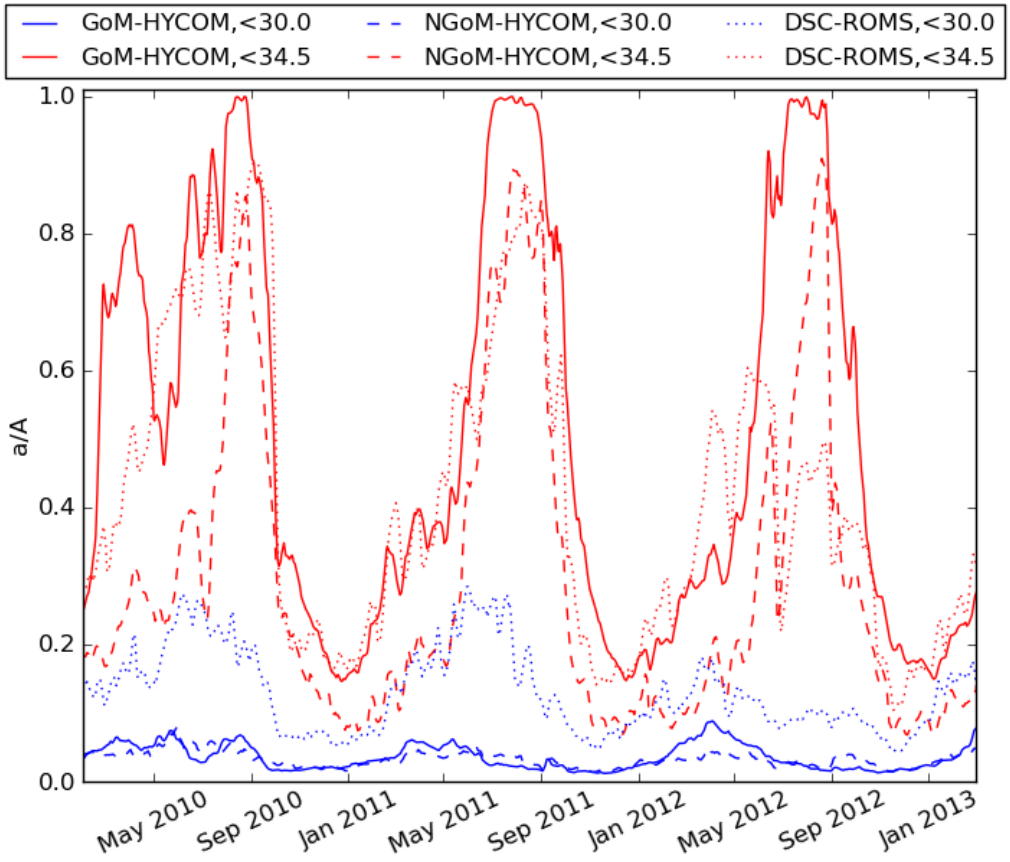

Figure 7: Area of the domain at the surface where SSS less than the values given in the legend, scaled by the total domain area (a/A), where a is area with SSS less than the values given in the legend and A is the total area of the ocean within the domain). DSC-ROMS has the greatest area of fresher riverine water (SSS<30.0) and GoM-HYCOM the greatest total area of riverine influenced water (SSS<34.5).

DSC-ROMS and then NGoM-HYCOM. The largest area of riverine water (SSS<34.5) for GoM-HYCOM may suggest that horizontal spreading and/or mixing processes are stronger in this model. In addition, the relaxation of surface salinity to climatology present in GoM-HYCOM enhances the presence of a low salinity pool along the northern Gulf. Note that in all models there is more fresh water in summer than in winter (Figures

525 3, 4 and 7), which is consistent with reported seasonal variability (Walker et al., 1996;
526 Morey et al., 2003; Androulidakis & Kourafalou, 2013). It should be noted, however, that
527 while the areal extent measured quantifies the area of low salinity and riverine-influenced
528 water in the region, it cannot be used independently to determine similarity in shape of
529 the riverine water. Instead it must be coupled with a visual inspection and/or an MHD
530 analysis to determine the shape and location of the contours. This highlights the
531 advantage of the MHD for automation of the quantification of the similarity in shape
532 between the contours without the need for visual inspection.

533 **5 Discussion and Summary**

534 Borrowing from the field of topology, the MHD has been introduced and
535 demonstrated as a tool for quantitative comparison of ocean model fields to satellite
536 remotely sensed data. This approach provides a method to quantify the agreement in
537 shape and spatial structure between fields of either similar or different but related
538 variables as well as producing an empirical relationship between the variables. Typically
539 in ocean modeling, satellite optical data have been used to qualitatively compare features
540 in geophysical fields that are known to manifest changes in the ocean color. By focusing
541 on shape characteristics, the MHD showcased here provides a numerical metric to
542 complement this qualitative comparison.

543 The applicability of the MHD has been demonstrated in this work through an
544 analysis of the agreement of the temporal and spatial variability of modeled SSS contours
545 with satellite OCI contours in the vicinity of a large river. A large number of MHD
546 values have been calculated for pairings of multiple SSS and OCI levels at eight-day

intervals over a three-year time span, and this information has been condensed into a set of best OCI-SSS pairings for each model. These provide a means to evaluate how well different models simulate the spatial structure and temporal evolution of the salinity field, and to better understand systematic differences (biases) between the models.

Specific differences among the tested models revealed by the MHD analysis include: 1) Lower salinity water is found further offshore in the DSC-ROMS model than in either of the HYCOM models as revealed by the closer matches between lower SSS contour values and the higher OCI contour values that are typically further from the river source. 2) SSS contours for GoM-HYCOM are more broadly spaced than in DSC-ROMS and NGoM-HYCOM as shown by the slower variation of SSS with OCI for the relationship inferred by the set of best pairings. 3) NGoM-HYCOM has the best overall match between the shapes of contours of surface salinity and OCI, followed closely by the GoM-HYCOM and then the DSC-ROMS as shown by the lowest MHD values in the optimum SSS-OCI relationships calculated for each model. These results agree with the visual analysis of the SSS fields and provide a quantitative assessment of the comparison between the models and observations. Furthermore, these findings are in agreement with the ability of NGoM-HYCOM to represent details in the development and evolution of the Mississippi River plume (Androulidakis et al., 2015), as evidenced from comparisons with various other data sources (e.g. Kourafalou and Androulidakis, 2013; Smith et al., 2016).

There are many factors that can affect the simulation of a river plume in models with different numerics and configurations. Important differences between models that impact the dynamics and horizontal spreading of a river plume include among other factors

surface forcing (data sources and flux calculations), river parameterization, horizontal and vertical mixing parameterizations, and spatial resolution. For example, the river parameterization in DSC-ROMS prescribes a lateral flux of volume and momentum of fresh water, whereas GoM-HYCOM relaxes the surface salinity in a region surrounding the river source, which is distributed with depth, and NGoM-HYCOM further corrects the pressure to account for the mass influx. The momentum and volume fluxes at the river source may be responsible for the greater offshore penetration of the very low salinity water in DSC-ROMS compared to the two HYCOM simulations. Alternatively, river discharge rates are prescribed differently among the models, which may also account for these differences. The coarser spatial resolution for GoM-HYCOM may lead to more horizontal diffusion and hence weaker salinity gradients inferred from the MHD analysis. A sound investigation of these influences is beyond the scope of this study. However, the MHD offers a diagnostic that would be highly advantageous for such an analysis as it permits objective quantitative skill assessment across models with different river parameterizations and/or within one model for sensitivity testing.

The MHD values for the best contour pairings indicate that GoM-HYCOM and NGoM-HYCOM have a closer match overall in shape of SSS contours with the satellite OCI contours in comparison to the DSC-ROMS model. As GOM-HYCOM is data assimilative, it most likely better represents the mesoscale features that transport low salinity water. NGoM-HYCOM also benefits from the good representation of these features, as it is nested within GoM-HYCOM. Both NGoM-HYCOM and DSC-ROMS are free-running models nested in data-assimilative ocean models. Differences in the nesting procedures, the location of the nesting boundaries and the product the model is

593 nested in may impact how the outer model constrains the mesoscale eddy influences.
594 Significant effort has been placed on parameterization of river inflow in the NGoM-
595 HYCOM, which has been previously assessed with in situ SSS measurements (e.g.
596 Kourafalou and Androulidakis, 2013; Androulidakis and Kourafalou, 2013; Ghani et al.,
597 2014). These are important factors for achieving a better match in shape to the satellite
598 optical observations.

599 Though the surface salinity in the vicinity of large rivers is linked to structures
600 evident in satellite ocean color imagery, it is important to note that without robust
601 analysis of in situ measurements within the specific region of study one cannot determine
602 which model's agreement to the satellite data is truly "best". In an example of such an
603 exercise, Chaichitehrani et al. (2014) derived CDOM and SSS relationships from *in situ*
604 observations which were used to calculate CDOM from a numerical model SSS output.
605 The model-derived CDOM was compared to satellite-derived CDOM qualitatively and
606 the model-derived values used to study the factors that affect CDOM distribution. With
607 the MHD, an additional step could be included which would allow quantitative
608 comparison of the satellite-derived CDOM with the model-derived CDOM and
609 determination of an empirical relationship.

610 Application of the MHD analysis technique to synoptic maps of salinity produced
611 from *in situ* surveys could yield functional relationships between OCI and SSS that could
612 enhance the utility of this procedure to evaluate models. Another benefit of the MHD
613 metric is that it can also be readily used to evaluate model fields with satellite
614 observations of the same variable providing valuable information on the simulated spatio-
615 temporal evolution of the surface fields, even when significant biases exist between the

model and satellite observations, as is now commonly the case with simulated biogeochemical fields as well as satellite salinity observations. Furthermore, the MHD provides the comparison between the datasets without the need for visual inspection, allowing automation, as well as quantification. Finally, since the MHD provides a robust metric indicating the agreement between simulated variables and observations, it may be possible to utilize this metric to construct a cost function to be used in an adjoint data assimilation method, allowing assimilation of a wealth of satellite data that are presently underutilized in ocean modeling.

Acknowledgements

This research was made possible by grants from the Bureau of Ocean Energy Management (BOEM) (M12PC00003) and the Gulf of Mexico Research Initiative, and the U.S. NASA (NNX14AM63G and NNX14AL98G). DSC-ROMS and NGoM-HYCOM model data are publicly available through the Gulf of Mexico Research Initiative Information and Data Cooperative (GRIIDC) at https://data.gulfresearchinitiative.org (UDI: R1.x138.080:0022, UDI: R1.x138.080:0008). The authors would also like to thank Dr. Matthew K. Howard at Texas A&M University for providing river data for the DSC-ROMS simulation and the HYCOM Consortium for providing access to the GoM-HYCOM data at www.hycom.org.

Appendix A. Fitted OCI-SSS Functional Relationships

For each model, a quadratic function is fit to all of the best pairings including both those derived from the OCI that yields the minimum MHD for a given SSS and those derived from the SSS that yields the minimum MHD for a given OCI (both plus and circle symbols in Figure 6). Pairings corresponding the minimum and maximum SSS and OCI values considered in the analysis (boundary rows and columns in Figure 6a-d) are excluded to avoid limiting cases impacting the fit. The quadratic functions are constrained to be monotonic over the range of SSS and OCI values tested. The resulting quadratic functions fit to the optimum pairings are:

$$\text{GoM-HYCOM: } OCI = -0.11\,(SSS)^2 + 5.42\,(SSS) - 53.63 \qquad \text{(A.1)}$$

$$\text{NGoM-HYCOM: } OCI = -0.38\,(SSS)^2 + 23.01\,(SSS) - 337.02 \qquad \text{(A.2)}$$

$$\text{DSC-ROMS: } OCI = -0.04\,(SSS)^2 + 1.30\,(SSS) - 1.26 \qquad \text{(A.3)}$$

6 References

Androulidakis, Y.S., V.H. Kourafalou and R. Schiller, 2015. Process studies on the Mississippi River plume: impact of topography, wind and discharge conditions. *Continental Shelf Research,* 107, 33-49.

Androulidakis, Y. S., & Kourafalou, V. H. (2013). On the processes that influence the transport and fate of Mississippi waters under flooding outflow conditions. *Ocean Dynamics, 63* (2-3), 143-164.

Binding, C., & Bowers, D. (2003). Measuring the salinity of the Clyde Sea from remotely sensed ocean colour. *Estuarine Coastal and Shelf Science, 57*, 605-611.

Bleck, R. (2002). An oceanic general circulation model framed in hybrid isopycnic-cartesian coordinates. *Ocean Modelling, 4*, 55-88.

Blondeau-Patissier, D., Gower, J. F., Dekker, A. G., Phinn, S. R., & Brando, V. E. (2014). A review of ocean color remote sensing methods and statistical techniques for the detection, mapping and analysis of phytoplankton blooms in coastal and open oceans. *Progress in Oceanography, 123*, 124-144.

Brekke, C., & Solberg, A. H. (2005). Oil spill detection by satellite remote sensing. *Remote Sensing of Environment, 95*, 1-13.

Chaichitehrani, N., D'Sa, E. J., Ko, D. S., Walker, N. D., Osburn, C. L., & Chen, R. F. (2014). Colored Dissolved Organic Matter Dynamics in the Northern Gulf of Mexico from Ocean Color and Numerical Model Results. *Journal of Coastal Research, 30* (4), 800-814.

671 Chassignet, E. P., Hurlburt. H. E., Smedstad, O. M., Barron, C. N., Ko, D. S., Rhodes, R.
672 C., et al. (2005). Assessment of data assimilative ocean models in the Gulf of Mexico
673 using ocean color. In W. Sturges, & A. Lugo-Fernadez (Eds.), *AGU Monograph Series*
674 (Vol. 161, pp. 87-100).

675 Chassignet, E. P., Smith, L. T., Halliwell, G. R., & Bleck, R. (2003). North Atlantic
676 Simulations with the Hybrid Coordinate Ocean Model (HYCOM): Impact of the Vertical
677 Coordinate Choice, Reference Pressure, and Thermobaricity. *Journal of Physical*
678 *Oceanography*, 2504-2526.

679 Chassignet, E., Hurlburt, H., Smedstad, O., Halliwell, G., Wallcraft, A., Metzger, E., et al.
680 (2006). Generalized vertical coordinates for eddy-resolving global and coastal ocean
681 forecasts. *Oceanography, 19* (1), 118-129.

682 Chonga, Y. J., Khana, A., Scheelbeeka, P., Butlerb, A., Bowersc, D., & Vineisa, P.
683 (2014). Climate change and salinity in drinking water as a global problem: using remote-
684 sensing methods to monitor surface water salinity. *International Journal of Remote*
685 *Sensing, 35* (4), 1585-1599.

686 Cummings, J. A. (2005). Operational multivariate ocean data assimilation. *Quarterly*
687 *Journal of the Royal Meteorological Society, 131*, 3583-3604.

688 Daoudi, M., Ghorbel, F., Mokadem, A., Avaro, O., & Sanson, H. (1999). Shape distances
689 for contour tracking and motion estimation. *Pattern Recognition, 32*, 1297-1306.

690 Dubuisson, M.-P., & Jain, A. (1994). A modified Hausdorff distance for object matching.
691 *Proceedings of the 12th IAPR International Conference on Pattern Recognition, 1994*, pp.
692 566-568.

693 Dukhovskoy, D. S., Ubnoske, J., Blanchard-Wrigglesworth, E., Hiester, H. R., &
694 Proshutinsky, A. (2015). Skill metrics for evaluation and comparison of sea ice models.
695 *Journal of Geophysical Research – Oceans*, 120(9), 5910-5931

696 Fairall, C. W., Bradley, E. F., Rogers, D. P., Edson, J. B., & Young, G. S. (1996). Bulk
697 parameterization of air-sea fluxes for tropical ocean-global atmosphere Coupled-Ocean
698 Atmosphere Response Experiment. *Journal of Geophysical Research,* 101, 3747-3764.

699 Ghani, M. H., Hole, L. R., Fer, I., Kourafalou, V. H., Wienders, N., & Peddie, D. (2014).
700 The SailBuoy remotely-controlled unmanned vessel: measurements of near surface
701 temperature, salinity and oxygen concentration in the Gulf of Mexico. *Methods in*
702 *Oceanography, 10*, 104-121.

703 Green, R. E., & Sosik, H M. (2004). Analysis of apparent optical properties and ocean
704 color models using measurements of seawater constituents in New England continental
705 shelf surface waters. *Journal of Geophysical Research, 109.*

706 Gregg, W. W. (2008). Assimilation of SeaWiFS ocean chlorophyll data into a three-
707 dimensional global ocean model. *Journal of Marine Systems, 69*, 205-225.

708 Gregg, W. W., Ginoux, P., Schopf, P., & Casey, N. W. (2003). Phytoplankton and iron:
709 validation of a global three-dimensional ocean biogeochemical model. *Deep Sea*
710 *Research Part II: Topical Studies in Oceanography, 50*, 3143-3169.

711 Hetland, R. D., & DiMarco, S. F. (2012). Skill assessment of a hydrodynamic model of
712 circulation over the Texas-Louisiana continental shelf. *Ocean Modelling, 43-44*, 64-76.

713 Hodur, R. M., Pullen, J., Cummings, J., Hong, X., Doyle, J. D., Martin, P., et al. (2002).
714 The Coupled Ocean/Atmosphere Mesoscale Prediction System (COAMPS).
715 *Oceanography, 15*, 88-98.

716 Hu, C., Barnes, B. B., Qi, L., & Corcoran, A. A. (2015a). A Harmful Algal Bloom of
717 Karenia brevis in the Northeastern Gulf of Mexico as Revealed by MODIS and VIIRS: A
718 Comparison. *Sensors, 15*, 2873-2887.

719 Hu, C., Murch, B., Corcoran, A. A., Zheng, L., Barnes, B. B., Weisberg, R. H., et al.
720 (2015b). Developing a Smart Semantic Web with Linked Data and Models for Near Real-
721 time Monitoring of Red Tides in the Eastern Gulf of Mexico. *IEEE Systems Journal, 99*,
722 1-9.

723 Hu, C., Lee, Z., & Franz, B. (2012). Chlorophyll algorithms for oligotrophic oceans: A
724 novel approach based on three-band reflectance difference. *Journal of Geophysical*
725 *Research, 117*, C01011.

726 Hu, C., Montgomery, E. T., Schmitt, R. W., & Muller-Karger, F. E. (2004). The dispersal
727 of the Amazon and Orinoco River water in the tropical Atlantic and Caribbean Sea:
728 Observation from space and S-PALACE floats. *Deep Sea Research II, 51*, 1151–1171.

729 Hu, C., Muller-Karger, F. E., Biggs, D. C., Carder, K. L., Nababan, B., Nadeau, D., and
730 Vanderbloemen, J. (2003), Comparison of ship and satellite bio-optical measurements on

731 the continental margin of the NE Gulf of Mexico, *International Journal of Remote*
732 *Sens*ing, 24, 2597-2612.

733 Huang, R. X. (1993). Real Freshwater Flux as a Natural Boundary Condition for the
734 Salinity Balance and Thermohaline Circulation Forced by Evaporation and Precipitation.
735 *Journal of Physical Oceanography, 23* (11), 2428-2446.

736 Huttenlocher, D., & Rucklidge, W. (1993). A multi-resolution technique for comparing
737 images using the Hausdorff distance. *1993 IEEE Computer Society Conference on*
738 *Computer Vision and Pattern Recognition*, 705-706.

739 Huttenlocher, D., Klanderman, G., & Rucklidge, W. (1993). Comparing images using the
740 Hausdorff distance. *IEEE Transactions on Pattern Analysis and Machine Intelligence, 15*,
741 850-863.

742 Kourafalou, V. H., & Androulidakis, Y. S. (2013). Influence of Mississippi induced
743 circulation on the Deepwater Horizon Oil Spill transport. *Journal of Geophysical*
744 *Research, 118*, 1-20.

745 Kourafalou, V. H., Peng, H., Kang, H., Hogan, P. J., M., S. O., & Weisberg, R. H. (2009).
746 Evaluation of Global Ocean Data Assimilation Experiment products on South Florida
747 nested simulations with the Hybrid Coordinate Ocean Model. *Ocean Dynamics, 59* (1),
748 47-66.

749 Large, W. G., McWilliams, J. C., & Doney, S. C. (1994). Oceanic vertical mixing: A
750 review and a model with a nonlocal boundary layer parameterization. *Reviews of*
751 *Geophysics, 32*, 363–403.

752 Liu, Y. Y., Weisberg, R. H., Hu, C. C., Kovach, C. C., & Riethmuller, R. R. (2013).
753 Evolution of the Loop Current System During the Deepwater Horizon Oil Spill Event as
754 Observed With Drifters and Satellites. In Y. Y. Liu, A. MacFadyen, Z.-G. Ji, & R. H.
755 Weisberg, *Monitoring and Modeling the Deepwater Horizon Oil Spill: A Record-*
756 *Breaking Enterprise* (pp. 91-101). American Geophysical Union.

757 Liu, Y., Weisberg, R. H., Hu, C., & Zheng, L. (2011). Tracking the Deepwater Horizon
758 Oil Spill: A Modeling Perspective. *Eos, Transactions American Geophysical Union, 92*,
759 45-46.

760 Mariano, A., Kourafalou, V. H., Srinivasan, A., Kang, H., Halliwell, G., Ryan, E., et al.
761 (2011). On the modeling of the 2010 Gulf of Mexico Oil Spill. *Dynamics of Atmospheres*
762 *and Oceans, 52*, 322-340.

763 Mattern, J. P., Fennel, K., & Dowd, M. (2010). Introduction and Assessment of Measures
764 for Quantitative Model-Data Comparison Using Satellite Images. *Remote Sensing, 2*,
765 794-818.

766 McClain, C. R. (2009). A Decade of Satellite Ocean Color Observations. *Annual Review*
767 *of Marine Science, 1*, 19-42.

768 Metzger, E. J., Smedstad, P. G., Thoppil, P. G., Hurlburt, H. E., Cummings, J. A.,
769 Wallcraft, A. J., et al. (2014). US Navy operational global ocean and Arctic ice prediction
770 systems. *Oceanography*, *27* (3), 32-43.

771 Morey, S. L., Martin, P. J., O'Brien, J. J., Wallcraft, A. A., & Zavala-Hidalgo, J. (2003a).
772 Export pathways for river discharged fresh water in the northern Gulf of Mexico. *Journal*
773 *of Geophysical Research: Oceans, 108*.

774 Morey, S. L., Schroeder, W. W., O'Brien, J. J., & Zavala-Hidalgo, J. (2003b). The annual
775 cycle of riverine influence in the eastern Gulf of Mexico basin. *Geophysical Research*
776 *Letters, 30*.

777 Morey, S. L., Zavala-Hidalgo, J., and O'Brien, J. J. (2005), The seasonal variability of
778 continental shelf circulation in the northern and western Gulf of Mexico from a high-
779 resolution numerical model, in Circulation of the Gulf of Mexico: Observations and
780 Models, *Geophysical Monograph Series. 161*, edited by W. Sturges and A. Lugo-
781 Fernandez, AGU, Washington, D. C., doi:10.1029/161GM16.

782 Muller-Karger, F. E., Smith, J. P., Werner, S., Chen, R., Roffer, M., Yanyun Liu, Y., et al.
783 (2015). Natural variability of surface oceanographic conditions in the offshore Gulf of
784 Mexico. *Progress in Oceanography*, 134, 54-76.

785 Nan, Z., Wang, S., Liang, X., Adams, T., Teng, W., & Liang, Y. (2010). Analysis of
786 Spatial Similarities Between NEXRAD and NLDAS Precipitation Data Products. *IEEE*
787 *Journal of Selected Topics in Applied Earth Observations and Remote Sensing, 3*, 371-
788 385.

789 Rosmond, T.E., Teixeira, J., Peng, M., Hogan, T. F., and Pauley, R., 2002, Navy
790 Operational Global Atmospheric Predictions System (NOGAPS): Forcing for ocean
791 models. *Oceanography, 15* (1), 99-108.

792 Rucklidge, W. J. (1997). Efficiently Locating Objects Using the Hausdorff Distance.
793 *International Journal of Computer Vision, 24*, 251-270.

794 Saha, S., Moorthi, S., Pan, H.-L., Wu, X., Wang, J., Nadiga, S., et al. (2010). The NCEP
795 Climate Forecast System Reanalysis. *Bulletin of the American Meteorological Society, 91*
796 (8), 1015-1057.

797 Schiller, R. V., Kourafalou, V. H., Hogan, P., & Walker, N. D. (2011). The dynamics of
798 the Mississippi River plume: Impact of topography, wind and offshore forcing on the fate
799 of plume waters. *Journal of Geophysical Research: Oceans, 116* (C6).

800 Schiller, R., & Kourafalou, V. (2010). Modeling river plume dynamics with the HYbrid
801 Coordinate Ocean Model . *Ocean Modelling, 33*, 101-117.

802 Shchepetkin, A. F., & McWilliams, J. (2003). A method for computing horizontal
803 pressure-gradient force in an oceanic model with a nonaligned vertical coordinate.
804 *Journal of Geophysical Research, 108* (C3).

805 Shchepetkin, A. F., & McWilliams, J. C. (2009). Correction and Commentary for "Ocean
806 Forecasting in Terrain-Following Coordinates: Formulation and Skill Assessment of the
807 Regional Ocean Modeling System" by Haidvogel et al., J. Comp. Phys. 227, pp. 3595-
808 3624. *Journal of Computational Physics, 228* (24), 8985-9000.

809 Shchepetkin, A. F., & McWilliams, J. C. (2005). The Regional Ocean Modeling System:
810 A split-explicit, free-surface, topography following coordinates ocean model. *Ocean*
811 *Modelling, 9*, 347-404.

812 Smith, S.R., K. Briggs, N. Lopez and V.H. Kourafalou, 2016. Numerical Model
813 Evaluation Using Automated Underway Ship Observations. *Journal of Atmospheric and*
814 *Oceanic Technology,* 33, 409-428.

815 Smolarkiewicz, P. K. (1983). A Simple Positive Definite Advection Scheme with Small
816 Implicit Diffusion. *Monthly Weather Review,* 111, 479-486.

817 Smolarkiewicz, P. K., & Clark, T. L. (1986). The multidimensional positive definite
818 advection transport algorithm: Further development and applications. *Journal of*
819 *Computational Physics, 67*, 396-438.

820 Song, Y., & Haidvogel, D. B. (1994). A semi-implicit ocean circulation model using a
821 generalized topography-following coordinate system. *Journal of Computational Physics,*
822 *115* (1), 228-244.

823 Stumpf, R. P., M.E. Culver, M., Tester, P., Tomlinson, M., Kirkpatrick, G., Pederson, B.
824 A., et al. (2003). Monitoring Karenia brevis blooms in the Gulf of Mexico using satellite
825 ocean color imagery and other data. *Harmful Algae, 2*, 147-160.

826 Venugopal, V., Basu, S., & Foufoula-Georgiou, E. (2005). A new metric for comparing
827 precipitation patterns with an application to ensemble forecasts. *Journal of Geophysical*
828 *Research: Atmospheres, D8*, 110.

829 Walker, N. D., Huh, O. K., Rouse, L. J., & Murray, S. P. (1996). Evolution and structure
830 of a coastal squirt off the Mississippi River delta: Northern Gulf of Mexico. *Journal of*
831 *Geophysical Research: Oceans,* 101, 20643-20655.

832 Walker, N. D., Wiseman, W. J., Rouse, L. J., & Babin, A. (2005). Effects of River
833 Discharge, Wind Stress, and Slope Eddies on Circulation and the Satellite-Observed
834 Structure of the Mississippi River. *Journal of Coastal Research*, 1228-1244.

835 Zhang, D., & Lu, G. (2004). Review of shape representation and description techniques.
836 *Pattern Recognition, 37*, 1-19.

837 Zhang, P., Wai, O., Chen, X., Lu, J., & Tian, L. (2014). Improving Sediment Transport
838 Prediction by Assimilating Satellite Images in a Tidal Bay Model of Hong Kong. *Water,*
839 *6*, 642-660.